ARTICLES
https://doi.org/10.1038/s41567-021-01329-6

nature physics

Tuning of dipolar interactions and evaporative cooling in a three-dimensional molecular quantum gas

Jun-Ru Li[1]✉, William G. Tobias[1], Kyle Matsuda[1], Calder Miller[1], Giacomo Valtolina[1,3], Luigi De Marco[1], Reuben R. W. Wang[1], Lucas Lassablière[2], Goulven Quéméner[2], John L. Bohn[1] and Jun Ye[1]✉

Ultracold polar molecules possess long-range, anisotropic and tunable dipolar interactions, providing opportunities to probe quantum phenomena that are inaccessible with existing cold gas platforms. However, experimental progress has been hindered by the dominance of two-body loss over elastic interactions, which prevents efficient evaporative cooling. Although recent work has demonstrated controlled interactions by confining molecules to a two-dimensional geometry, a general approach for tuning molecular interactions in a three-dimensional stable system has been lacking. Here we demonstrate tunable elastic dipolar interactions in a bulk gas of ultracold $^{40}K^{87}Rb$ molecules in three dimensions, facilitated by an electric field-induced shielding resonance that suppresses the reactive loss by a factor of 30. This improvement in the ratio of elastic to inelastic collisions enables direct thermalization. The thermalization rate depends on the angle between the collisional axis and the dipole orientation controlled by an external electric field, a direct manifestation of the anisotropic dipolar interaction. We achieve evaporative cooling mediated by the dipolar interactions in three dimensions. This work demonstrates full control of a long-lived bulk quantum gas system with tunable long-range interactions, paving the way for the study of collective quantum many-body physics.

The study of atomic quantum gases has benefited from precise control over the interactions between their constituents. By tuning the interactions with convenient tools such as external fields[1,2], one can vary the properties of a quantum system and explore its dynamics and phase transitions. Compared with atoms, polar molecules[3–6] possess large electric dipole moments and rich energy-level structures, making them a unique platform for studying a range of topics such as quantum magnetism[7–10], exotic superfluidity[11–13], dipolar collective dynamics[14–19], precision measurements[20,21], quantum sensing[22] and quantum information processing[23,24].

Elastic collisions play a critical role in many of these applications. Yet, so far, direct observation of the elastic collisions in three-dimensional (3D) ultracold molecular gases has been prevented by rapid collisional losses[25–29], even for molecular species without exothermic chemical reactions[27–29], although the mechanisms responsible are still under investigation[30–34]. The recent production of a degenerate Fermi gas of $^{40}K^{87}Rb$ (KRb) molecules led to the surprising discovery of suppressed reaction rates upon entering deep degeneracy[35,36], although the effect was observed at zero field where the dipolar elastic collisions vanish.

Turning on the dipolar interaction in a 3D geometry by applying an external electric field $\mathbf{E}$ to polarize the molecules leads to vastly enhanced losses as a result of dipolar attraction[26,37]. Although the collision cross-section of dipolar elastic collisions increases with the induced dipole moment d as d^4 (ref. [38]), reactive losses increase more strongly as d^6 (refs. [26,37]) for fermionic molecules, preventing the observation of any dynamics related to the elastic dipolar collisions. Inspired by earlier theory[39,40] and experimental work[41], we recently demonstrated that in quasi-two dimensions (quasi-2D)[42], where the geometry restricts the relative angles of colliding molecules, the two-body loss can be suppressed by more than a factor of 2 from the zero-field value, and strong elastic collisions dominate.

Despite the progress made in quasi-2D, a full 3D gas of polar molecules provides the most general platform for studying dipolar physics. Moreover, interaction effects associated with the long-range and anisotropic nature of the dipolar interaction are more prominent in 3D[43], leading to unique collective dynamics in bulk dipolar gases[14–18]. Therefore, the ability to tune the dipolar interaction in 3D while mitigating the strong two-body loss is of great experimental interest. Resonant shielding using d.c. electric fields, recently demonstrated in quasi-2D[44–46], is a promising approach for suppressing molecular loss in 3D. However, the properties of elastic collisions under the shielding were not experimentally studied. In another approach, two-body loss inside an optical tweezer was suppressed using a coherent microwave drive[47], yet with no study on elastic collisions either.

In this Article, we use resonant shielding to enable full control over the interactions between ultracold, reactive molecules in 3D, accessing a regime where elastic collisions are dominant. At a shielding field of $E_S = 12.72\,\mathrm{kV\,cm^{-1}}$, we observe a suppression of the two-body loss rate between molecules in the first excited rotational state by a factor of 30 below the background value and achieve a lifetime of ~10 s at typical densities n of $2.5\times10^{11}\,\mathrm{cm^{-3}}$. Enabled by the shielding, we quantitatively characterize elastic collisions in the system by performing cross-dimensional relaxation experiments after selectively heating along one trap axis of the molecular gas. An elastic-to-inelastic collision ratio γ of 12 is measured. We further show that the relaxation rate changes by a factor of 2.5 as we

[1]JILA, National Institute of Standards and Technology and Department of Physics, University of Colorado, Boulder, CO, USA. [2]Université Paris-Saclay, CNRS, Laboratoire Aimé Cotton, Orsay, France. [3]Present address: Fritz-Haber-Institut der Max-Planck-Gesellschaft, Berlin, Germany.
✉e-mail: junru.li@colorado.edu; Ye@jila.colorado.edu

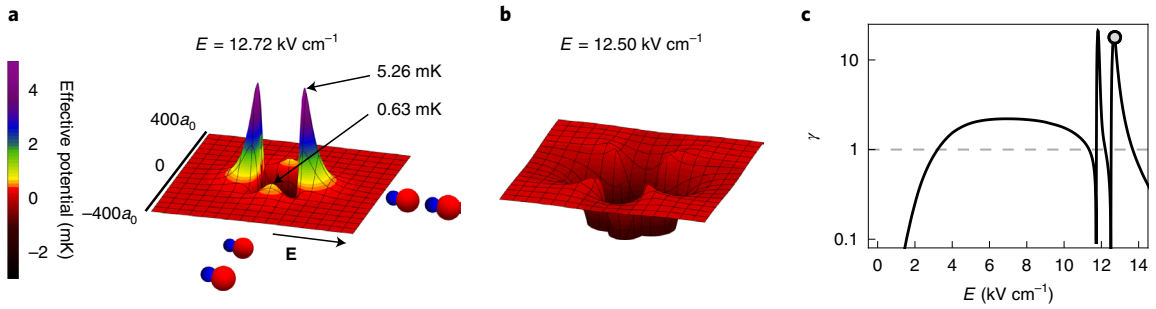

Fig. 1 | Effective intermolecular potential and tuning of molecular interactions near the shielding resonance. a,**b**, Calculated effective intermolecular potential for KRb in $|1,0\rangle$ at $E = 12.72\,\mathrm{kV\,cm^{-1}}$ (**a**) and $E = 12.50\,\mathrm{kV\,cm^{-1}}$ (**b**) (Supplementary Section 1). The resonant dipolar coupling mixes two degenerate collisional channels. The strong mixing between the channels modifies the effective intermolecular potential and results in either suppression or enhancement of the two-body loss rate depending on E. a_0 is the Bohr radius. **c**, Calculated ratio γ of the elastic rate to reactive rate for KRb in $|1,0\rangle$ at $T = 330\,\mathrm{nK}$ (ref. [45]). Our experiment is carried out at $E_S = 12.72\,\mathrm{kV\,cm^{-1}}$ (indicated by the grey circle) where $\gamma = 17.8$ is calculated. The grey dashed line indicates $\gamma = 1$.

vary the orientation of the dipoles relative to the direction of heating. Despite the presence of the shielding, our measurements of the elastic collisions are consistent with universal dipolar scattering[38,48]. Leveraging the large γ at $\mathbf{E}_S$, we perform efficient evaporative cooling in 3D, signalled by a gain in the phase-space density (PSD) as the particle number is reduced. Because the shielding mechanism is predicted to work for a broad class of molecular species[49], our strategy provides a general method for preparing low-entropy molecular samples with strong elastic dipolar interactions.

Our experiments are conducted with KRb in the excited rotational state $|N=1,m_N=0\rangle$ in a 3D optical dipole trap (ODT). Here, N is the field-dressed rotational quantum number and m_N is its projection onto the electric field $\mathbf{E}$. We prepare the molecular gases following the procedure described in ref. [35]. Briefly, we start with a degenerate mixture of ^{40}K and ^{87}Rb in an ODT. Molecules in $|0,0\rangle$ are created via magnetoassociation around 546.62 G followed by stimulated Raman adiabatic passage (STIRAP) at an electric field of $\mathbf{E}_{\mathrm{STIRAP}} = 4.5\,\mathrm{kV\,cm^{-1}}$. The molecules are transferred to $|1,0\rangle$ with a microwave Rabi π-pulse. For detection, molecules are transferred back to $|0,0\rangle$, dissociated to the Feshbach state, and imaged after time-of-flight expansion. The ODT has trapping frequencies of $(\omega_x,\omega_y,\omega_z) = 2\pi\times(45,250,40)\,\mathrm{Hz}$ for $|1,0\rangle$ at $\mathbf{E}_{\mathrm{STIRAP}}$, with weak dependence on $\mathbf{E}$ (Methods). In contrast to refs. [42,44], where only the lowest harmonic level along the tightly confined direction is dominantly populated, here we have $k_B T \gg \hbar\omega_i$ for all three directions, fulfilling the criterion of a 3D geometry ($\hbar$ is the reduced Planck constant and k_B is the Boltzmann constant).

Long-lived gases of polar molecules in 3D

The two-body loss of KRb in $|N=1,m_N=0\rangle$ is suppressed at certain electric fields by resonant collisional shielding[44–46]. The suppression arises from tuning collisional channels into degeneracy using $\mathbf{E}$, where they are mixed by the resonant dipolar coupling. The strength of the coupling depends on the spatial separation R between the two molecules. The resultant avoided crossing modifies the energy of the coupled channels and manifests as an effective intermolecular potential (Supplementary Section 1). At the centre of the resonance, $E_0 \approx 12.67\,\mathrm{kV\,cm^{-1}}$, the energy of the collision channel $|1,0\rangle|1,0\rangle$ is degenerate with that of $|0,0\rangle|2,0\rangle$, where the two kets represent the symmetrized rotational states of the pair of colliding molecules. In the vicinity of E_0, for $E > E_0$, the mixing results in a repulsive energy barrier for $|1,0\rangle|1,0\rangle$, preventing the molecules from getting close enough to undergo a chemical reaction. In contrast to the barrier formed by the direct dipolar interaction[26,37,40–42], the barrier formed by resonant shielding exists for both 'head-to-tail' and 'side-by-side' collisions, shown in Fig. 1a, enabling the suppression of two-body loss even in 3D. For $E < E_0$, the effective potential is mainly attractive, resulting in enhanced loss (Fig. 1b).

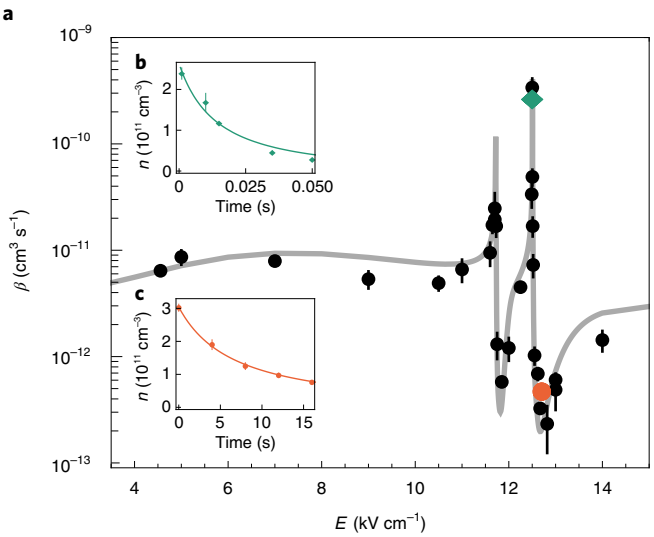

Fig. 2 | Resonant shielding of the reactive loss in 3D. a, Measured two-body loss rate versus electric field strength. The solid line is the theoretical calculation for the experimental condition $T = 330\,\mathrm{nK}$ with no free parameters. Error bars are 1 s.e. from fits to the two-body loss rate equation. The green diamond and orange circle identify the fields for which decay curves are plotted in **b** and **c**, respectively. **b**,**c**, Molecule loss measurements at $E = 12.50\,\mathrm{kV\,cm^{-1}}$ (**b**) and $12.72\,\mathrm{kV\,cm^{-1}}$ (**c**), where the loss is enhanced and suppressed, respectively. Solid lines are fits to the two-body loss rate equation. Error bars are 1 s.e. of three independent measurements.

We measure the shielding effect by monitoring the decay rate of the average molecular density n at different $\mathbf{E}$. To do so, $\mathbf{E}$ is ramped from $\mathbf{E}_{\mathrm{STIRAP}}$ to its target value in 60 ms after molecules in $|1,0\rangle$ are produced. We typically have 1.5×10^4 molecules in $|1,0\rangle$ at $T = 300\,\mathrm{nK}$, with $n = 2.5\times10^{11}\,\mathrm{cm^{-3}}$ after the field ramp. After a variable hold time t, $\mathbf{E}$ is ramped back to $\mathbf{E}_{\mathrm{STIRAP}}$ for imaging. The reactive two-body loss rate β is extracted by fitting the decay of n with $\dot{n} = -\beta n^2 - (3n/2T)\dot{T}$, where the first term is the reactive loss and the second term accounts for the temperature dependence of n. The resonant shielding effect manifests as two sharp features

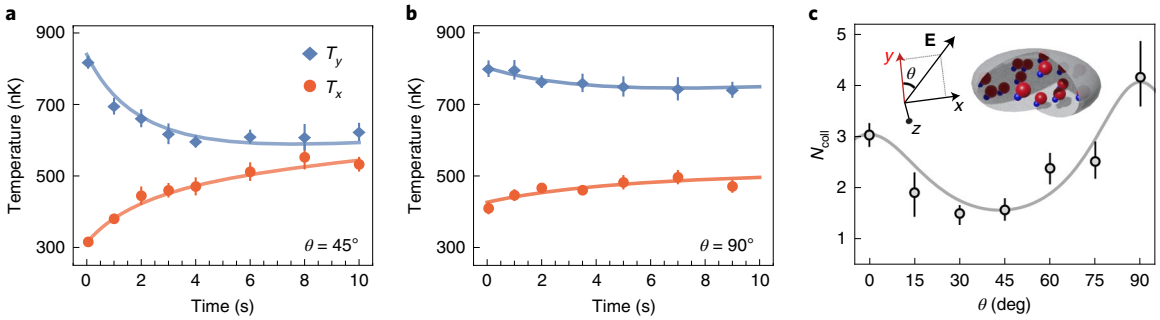

Fig. 3 | Anisotropic cross-dimensional thermalization of molecules via dipolar elastic collisions. a,**b**, Time evolution of the temperature for $\theta = 45°$ (**a**) and $\theta = 90°$ (**b**) after parametric heating along y. The solid lines are fits to our model (Methods). The thermalization is faster at $\theta = 45°$. T_z is not directly measured and is assumed to be the same as T_x during the entire process. Error bars represent 1 s.e. **c**, Angle-dependent number of collisions required for the rethermalization of dipolar Fermi gases. N_{coll} is extracted by fitting the time evolution of the temperature (Methods). The grey solid line represents the calculated analytical expression (equation (2)). Inset: geometry of the experiment. Molecules are polarized with a bias field **E** whose orientation angle θ is varied between 0° and 90° within the x–y plane. The molecular gases are heated parametrically along the y direction to create an initial condition of $T_y \approx 2.5T_x$, $T_x = T_z$.

in β around $E = 11.5\,\mathrm{kV\,cm^{-1}}$ and $12.5\,\mathrm{kV\,cm^{-1}}$, as shown in Fig. 2a. The two resonant features correspond to the coupled channels $|1,0\rangle|1,0\rangle \rightarrow |0,0\rangle|2,\pm1\rangle$ and $|1,0\rangle|1,0\rangle \rightarrow |0,0\rangle|2,0\rangle$, respectively. The width of each feature is $\sim 100\,\mathrm{V\,cm^{-1}}$, determined by the differential dipole moments of the rotational states involved and the strength of the dipolar coupling (Supplementary Section 1). Near the resonances, β varies by three orders of magnitude within a change of E of $0.25\,\mathrm{kV\,cm^{-1}}$. Two decay curves exemplifying this contrast are displayed in Fig. 2b,c. At $E_S = 12.72\,\mathrm{kV\,cm^{-1}}$, we observe long-lived (~10 s) molecular gases in 3D (Fig. 2b). When E is tuned far from the resonances, β increases with d, similar to KRb in $|0,0\rangle$ (ref. [26]). At $E = 4.5\,\mathrm{kV\,cm^{-1}}$, where the molecules have a similar dipole moment as at E_S, the lifetime is much shorter (~1 s), highlighting the prominent effect of resonant dipolar shielding on the two-body loss.

Elastic collisions between molecules in 3D

This long-lived molecular gas offers a practical platform to explore the effect of dipolar elastic collisions between reactive molecules. The elastic collisions occur at rate $n\sigma_{el}v$, where σ_{el} is the elastic cross-section and v is the ensemble-averaged relative collisional velocity of two molecules (Methods). Neglecting the effects of resonant shielding, the molecule–molecule elastic cross-section σ_{el} for indistinguishable fermionic molecules is predicted to vary only with d in the ultracold regime, approaching a universal value $\sigma_{el} = (32\pi/15)a_d^2$ (ref. [38]). Here, $a_d = (m/2)d^2/(4\pi\varepsilon_0\hbar^2)$ and m is the mass of the molecule. At E_S, KRb in $|1,0\rangle$ has $d = -0.08\,\mathrm{D}$ and the universal theory predicts $\sigma_{el} = 2.8 \times 10^{-12}\,\mathrm{cm^2}$.

The resonant dipolar coupling modifies the effective intermolecular potential and hence also modifies the properties of the elastic collisions. The effects depend not only on E but also on the statistics of the molecules, which affects the short-range interactions. For fermionic $^{40}K^{87}Rb$, this effect is manifested as a sharp enhancement in σ_{el} as the resonance is approached from lower E, although γ remains low due to the enhanced loss. At E_s, where the loss is suppressed, σ_{el} is predicted to deviate only slightly from the universal value[45]. Calculations[45] yield $\gamma = 17.8$ at $T = 330\,\mathrm{nK}$ (Fig. 1c), large enough for thermalization within the ensemble lifetime.

We experimentally demonstrate and characterize the elastic collisions through cross-dimensional thermalization, with the geometry shown in Fig. 3c. The molecular gas is heated along the more tightly confining y direction. Elastic collisions redistribute the excess kinetic energy from y to x and z. The rate Γ_{th} of this relaxation process is proportional to the elastic collision rate as

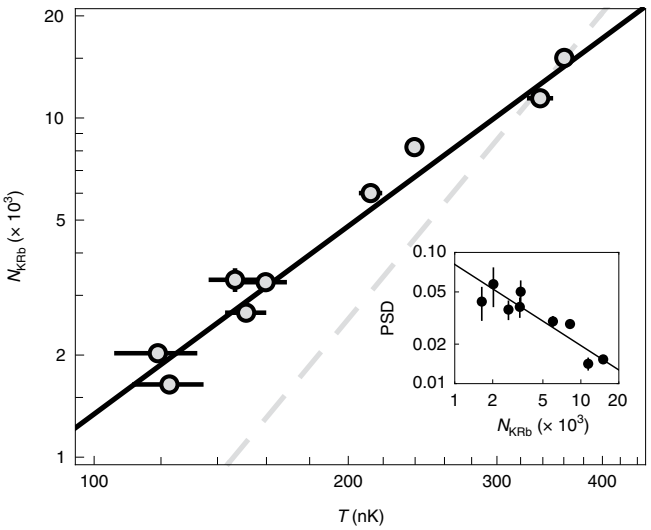

Fig. 4 | Efficient evaporative cooling of reactive polar molecules in 3D. Evolution of N_{KRb} and T at different stages of the evaporation at E_S and with $\theta = 0°$. The power-law fit (black line) yields $S_{evap} = 1.84(9)$, indicating efficient evaporation. The grey dashed line represents a constant PSD. Error bars indicate 1 s.e. Inset: PSD ($N_{KRb}(\hbar\bar{\omega}/k_BT)^3$) versus N_{KRb} during evaporation, displaying a clear gain. Here, $\bar{\omega}$ is the geometric mean of the trapping frequencies.

$$\Gamma_{th} = \frac{n\sigma_{el}v}{N_{coll}}. \quad (1)$$

Here, factor N_{coll} is physically interpreted as the number of collisions required to thermalize. N_{coll} has been calculated to be 2.7 and 4.1 for s-wave[50] and p-wave[51] collisions, respectively. For dipolar elastic collisions, theoretical calculations[48] and experiments with magnetic atoms[52,53] have shown that N_{coll} depends on the angle θ between the dipole and the direction of heating y. This is a direct result of the anisotropic dipolar collisions.

We observe the anisotropic elastic relaxation process using the following experimental procedure. The molecules are initially prepared in thermal equilibrium in $|1,0\rangle$ at $E_S = 12.72\,\mathrm{kV\,cm^{-1}}$ with $\theta = 0°$. The field is then rotated to the target angle θ in 60 ms. Next, a

temperature imbalance between the trap axes is introduced by parametrically heating the molecular cloud along y for 50–100 ms (inset, Fig. 3c), which is much shorter than the timescale of thermalization. We create an initial condition of $T_y \approx 2.5T_x$. The relaxation process is observed by monitoring the time evolution of T_y and T_x as the sample thermalizes in the trap.

As the gas equilibrates, the temperatures approach each other. The temperature evolution for $\theta = 45°$ and $\theta = 90°$ is shown in Fig. 3a and 3b, respectively. A clear difference in the thermalization rates for the two orientation angles is observed. We quantitatively study the relaxation by fitting the time evolution of T_x, T_y and n with a set of coupled differential equations (Methods and Extended Data Fig. 1). The equations capture two physical processes contributing to the temperature change: the elastic dipolar collisions associated with N_{coll}, and the reactive loss, associated with the loss coefficient K_{L}, which preferentially removes two colliders with high relative kinetic energy[26]. Here, K_{L} is related to β as $K_{\mathrm{L}} = (1/3)\beta/T$ for a thermally equilibrated gas at temperature T.

For each θ, we extract N_{coll} and K_{L} from the fits (Methods and Extended Data Fig. 1). Because the thermalization rate depends on $\sigma_{\mathrm{el}}/N_{\mathrm{coll}}$, we use $\sigma_{\mathrm{el}} = 2.8 \times 10^{-12}\,\mathrm{cm}^2$ in our analysis to extract N_{coll}. We observe a clear angular dependence of the number of collisions required for thermalization, summarized in Fig. 3c. At 45°, only $1.6^{+0.2}_{-0.1}$ collisions are required for thermalization, whereas $4.1^{+0.9}_{-0.6}$ collisions are required for $\theta = 90°$. In the limit of small parametric excitation and using the scattering cross-section of point dipoles, N_{coll} can be calculated analytically within the Enskog formalism[54]. Within this formalism, the collective behaviour of a thermal gas is studied by observing only the phase-space-averaged values of relevant quantities (for example, the width of the gas cloud) over time, offering a simplification over tracking all molecular degrees of freedom. Adopting the computational techniques used in refs. [54,55] permits the following concise analytic expression:

$$N_{\mathrm{coll}}(\theta) \approx \frac{97.4}{45 + 4\cos 2\theta - 17\cos 4\theta} \qquad (2)$$

for a gas heated along y and rethermalization measured along x. More details of the derivation are provided in Supplementary Section 2. Equation (2) (grey solid curve, Fig. 3c) describes the measured angular dependence quite well, despite the approximations above. From the measured K_{L}, we calculate $\gamma = \sigma_{\mathrm{el}} v/(3K_{\mathrm{L}}T)$ as high as 12(1), confirming the dominant role of the elastic collisions in the observed temperature evolution. Our measurements now establish the fact that characteristics of the direct dipolar interaction are preserved at E_{s}, suggesting that molecules at the shielding field provide a general platform for realizing stable and strongly dipolar systems.

Evaporative cooling of molecules in 3D

A large γ enables direct evaporative cooling of KRb in 3D. Moreover, the Wigner threshold law[25,56] suggests γ will increase further at lower temperatures for fermionic molecules as $\gamma \sim 1/\sqrt{T}$, which facilitates the evaporative cooling processes. We perform evaporation by lowering the depth of the optical trap at $\theta = 0°$. During evaporation, we observe that the x and y directions remain in equilibrium and the temperature T drops along with the number of molecules N_{KRb} remaining in the trap. Efficient evaporation requires the slope $S_{\mathrm{evap}} = \partial \ln N_{\mathrm{KRb}}/\partial \ln T$ to be smaller than 3 in 3D. We measure $S_{\mathrm{evap}} = 1.84(9)$, significantly below this threshold (Fig. 4). As N_{KRb} decreases, the PSD increases from 0.014(1) to 0.06(2), corresponding to a decrease of T/T_{F} from 2.3(1) to 1.4(2) (T_{F} is the Fermi temperature).

Compared with the procedure in ref. [35], which produced a degenerate Fermi gas at $T/T_{\mathrm{F}} = 0.3$ with $N_{\mathrm{KRb}} = 2.5 \times 10^4$, the present approach requires preparing molecules in $|1,0\rangle$ at E_{S}. This requires a ramp of the electric field that causes molecular loss and heating, limiting the highest PSD achieved in this work. Future technical improvements, such as direct creation of molecules at E_{S}, will enable evaporation of molecular gases to deep quantum degeneracy. The efficiency of the evaporative cooling demonstrated here is limited by the relatively small γ achievable in KRb. For molecules such as ^{23}Na^{133}Cs, the same approach should allow $\gamma > 1 \times 10^6$ at moderate electric fields around 2.5 kV cm^{-1} (ref. [49]), enabling more efficient evaporation.

Our work highlights a general approach for controlling the interaction properties of polar molecules in 3D and demonstrates a promising strategy for producing low-entropy molecular gases in bulk systems. Such capabilities are essential for a broad range of applications in molecule-based quantum platforms, such as the study of exotic many-body quantum phases in dipolar quantum gases.

Online content

Any methods, additional references, Nature Research reporting summaries, source data, extended data, supplementary information, acknowledgements, peer review information; details of author contributions and competing interests; and statements of data and code availability are available at https://doi.org/10.1038/s41567-021-01329-6.

Received: 19 May 2021; Accepted: 15 July 2021;
Published online: 2 September 2021

References

1. Chin, C., Grimm, R., Julienne, P. & Tiesinga, E. Feshbach resonances in ultracold gases. *Rev. Mod. Phys.* **82**, 1225–1286 (2010).
2. Saffman, M., Walker, T. G. & Mølmer, K. Quantum information with Rydberg atoms. *Rev. Mod. Phys.* **82**, 2313–2363 (2010).
3. Ni, K.-K. et al. A high phase-space-density gas of polar molecules. *Science* **322**, 231–235 (2008).
4. Quéméner, G. & Julienne, P. S. Ultracold molecules under control! *Chem. Rev.* **112**, 4949–5011 (2012).
5. Carr, L. D., DeMille, D., Krems, R. V. & Ye, J. Cold and ultracold molecules: science, technology and applications. *New J. Phys.* **11**, 055049 (2009).
6. Bohn, J. L., Rey, A. M. & Ye, J. Cold molecules: progress in quantum engineering of chemistry and quantum matter. *Science* **357**, 1002–1010 (2017).
7. Gorshkov, A. V. et al. Quantum magnetism with polar alkali-metal dimers. *Phys. Rev. A* **84**, 033619 (2011).
8. Peter, D., Müller, S., Wessel, S. & Büchler, H. P. Anomalous behavior of spin systems with dipolar interactions. *Phys. Rev. Lett.* **109**, 025303 (2012).
9. Yan, B. et al. Observation of dipolar spin-exchange interactions with lattice-confined polar molecules. *Nature* **501**, 521–525 (2013).
10. Yao, N. Y., Zaletel, M. P., Stamper-Kurn, D. M. & Vishwanath, A. A quantum dipolar spin liquid. *Nat. Phys.* **14**, 405–410 (2018).
11. Cooper, N. R. & Shlyapnikov, G. V. Stable topological superfluid phase of ultracold polar fermionic molecules. *Phys. Rev. Lett.* **103**, 155302 (2009).
12. Pikovski, A., Klawunn, M., Shlyapnikov, G. V. & Santos, L. Interlayer superfluidity in bilayer systems of fermionic polar molecules. *Phys. Rev. Lett.* **105**, 215302 (2010).
13. Baranov, M. A., Mar'enko, M. S., Rychkov, V. S. & Shlyapnikov, G. V. Superfluid pairing in a polarized dipolar Fermi gas. *Phys. Rev. A* **66**, 013606 (2002).
14. Baranov, M. A., Dalmonte, M., Pupillo, G. & Zoller, P. Condensed matter theory of dipolar quantum gases. *Chem. Rev.* **112**, 5012–5061 (2012).
15. Ronen, S. & Bohn, J. L. Zero sound in dipolar Fermi gases. *Phys. Rev. A* **81**, 033601 (2010).
16. Fregoso, B. M. & Fradkin, E. Ferronematic ground state of the dilute dipolar Fermi gas. *Phys. Rev. Lett.* **103**, 205301 (2009).
17. Wilson, R. M., Ronen, S. & Bohn, J. L. Critical superfluid velocity in a trapped dipolar gas. *Phys. Rev. Lett.* **104**, 094501 (2010).
18. Liu, B., Li, X., Yin, L. & Liu, W. V. Weyl superfluidity in a three-dimensional dipolar Fermi gas. *Phys. Rev. Lett.* **114**, 045302 (2015).
19. Babadi, M. & Demler, E. Collective excitations of quasi-two-dimensional trapped dipolar fermions: transition from collisionless to hydrodynamic regime. *Phys. Rev. A* **86**, 063638 (2012).
20. Andreev, V. et al. Improved limit on the electric dipole moment of the electron. *Nature* **562**, 355–360 (2018).
21. Cairncross, W. B. & Ye, J. Atoms and molecules in the search for time-reversal symmetry violation. *Nat. Rev. Phys.* **1**, 510–521 (2019).

22. Bilitewski, T. et al. Dynamical generation of spin squeezing in ultracold dipolar molecules. *Phys. Rev. Lett.* **126**, 113401 (2021).
23. André, A. et al. A coherent all-electrical interface between polar molecules and mesoscopic superconducting resonators. *Nat. Phys.* **2**, 636–642 (2006).
24. Ni, K.-K., Rosenband, T. & Grimes, D. D. Dipolar exchange quantum logic gate with polar molecules. *Chem. Sci.* **9**, 6830–6838 (2018).
25. Ospelkaus, S. et al. Quantum-state controlled chemical reactions of ultracold potassium–rubidium molecules. *Science* **327**, 853–857 (2010).
26. Ni, K.-K. et al. Dipolar collisions of polar molecules in the quantum regime. *Nature* **464**, 1324–1328 (2010).
27. Takekoshi, T. et al. Ultracold dense samples of dipolar RbCs molecules in the rovibrational and hyperfine ground state. *Phys. Rev. Lett.* **113**, 205301 (2014).
28. Guo, M. et al. Creation of an ultracold gas of ground-state dipolar $^{23}Na^{87}Rb$ molecules. *Phys. Rev. Lett.* **116**, 205303 (2016).
29. Park, J. W., Will, S. A. & Zwierlein, M. W. Ultracold dipolar gas of fermionic $^{23}Na^{40}K$ molecules in their absolute ground state. *Phys. Rev. Lett.* **114**, 205302 (2015).
30. Mayle, M., Quéméner, G., Ruzic, B. P. & Bohn, J. L. Scattering of ultracold molecules in the highly resonant regime. *Phys. Rev. A* **87**, 012709 (2013).
31. Christianen, A., Zwierlein, M. W., Groenenboom, G. C. & Karman, T. Photoinduced two-body loss of ultracold molecules. *Phys. Rev. Lett.* **123**, 123402 (2019).
32. Gregory, P. D., Blackmore, J. A., Bromley, S. L. & Cornish, S. L. Loss of ultracold $^{87}Rb^{133}Cs$ molecules via optical excitation of long-lived two-body collision complexes. *Phys. Rev. Lett.* **124**, 163402 (2020).
33. Liu, Y. et al. Photo-excitation of long-lived transient intermediates in ultracold reactions. *Nat. Phys.* **16**, 1132–1136 (2020).
34. Hu, M.-G. et al. Direct observation of bimolecular reactions of ultracold KRb molecules. *Science* **366**, 1111–1115 (2019).
35. De Marco, L. et al. A degenerate Fermi gas of polar molecules. *Science* **363**, 853–856 (2019).
36. Tobias, W. G. et al. Thermalization and sub-Poissonian density fluctuations in a degenerate molecular Fermi gas. *Phys. Rev. Lett.* **124**, 033401 (2020).
37. Quéméner, G. & Bohn, J. L. Strong dependence of ultracold chemical rates on electric dipole moments. *Phys. Rev. A* **81**, 022702 (2010).
38. Bohn, J. L., Cavagnero, M. & Ticknor, C. Quasi-universal dipolar scattering in cold and ultracold gases. *New J. Phys.* **11**, 055039 (2009).
39. Micheli, A. et al. Universal rates for reactive ultracold polar molecules in reduced dimensions. *Phys. Rev. Lett.* **105**, 073202 (2010).
40. Quéméner, G. & Bohn, J. L. Dynamics of ultracold molecules in confined geometry and electric field. *Phys. Rev. A* **83**, 012705 (2011).
41. de Miranda, M. H. G. et al. Controlling the quantum stereodynamics of ultracold bimolecular reactions. *Nat. Phys.* **7**, 502–507 (2011).
42. Valtolina, G. et al. Dipolar evaporation of reactive molecules to below the Fermi temperature. *Nature* **588**, 239–243 (2020).
43. Lahaye, T., Menotti, C., Santos, L., Lewenstein, M. & Pfau, T. The physics of dipolar bosonic quantum gases. *Rep. Prog. Phys.* **72**, 126401 (2009).
44. Matsuda, K. et al. Resonant collisional shielding of reactive molecules using electric fields. *Science* **370**, 1324–1327 (2020).
45. Wang, G. & Quéméner, G. Tuning ultracold collisions of excited rotational dipolar molecules. *New J. Phys.* **17**, 035015 (2015).
46. Avdeenkov, A. V., Kajita, M. & Bohn, J. L. Suppression of inelastic collisions of polar $^1\Sigma$ state molecules in an electrostatic field. *Phys. Rev. A* **73**, 022707 (2006).
47. Anderegg, L. et al. Observation of microwave shielding of ultracold molecules. *Science* **373**, 779–782 (2021).
48. Bohn, J. L. & Jin, D. S. Differential scattering and rethermalization in ultracold dipolar gases. *Phys. Rev. A* **89**, 22702 (2014).
49. González-Martínez, M. L., Bohn, J. L. & Quéméner, G. Adimensional theory of shielding in ultracold collisions of dipolar rotors. *Phys. Rev. A* **96**, 032718 (2017).
50. Monroe, C. R., Cornell, E. A., Sackett, C. A., Myatt, C. J. & Wieman, C. E. Measurement of Cs–Cs elastic scattering at $T = 30\,\mu K$. *Phys. Rev. Lett.* **70**, 414–417 (1993).
51. DeMarco, B., Bohn, J. L., Burke, J. P., Holland, M. & Jin, D. S. Measurement of *p*-wave threshold law using evaporatively cooled fermionic atoms. *Phys. Rev. Lett.* **82**, 4208–4211 (1999).
52. Aikawa, K. et al. Anisotropic relaxation dynamics in a dipolar Fermi gas driven out of equilibrium. *Phys. Rev. Lett.* **113**, 263201 (2014).
53. Tang, Y., Sykes, A., Burdick, N. Q., Bohn, J. L. & Lev, B. L. *s*-wave scattering lengths of the strongly dipolar bosons ^{162}Dy and ^{164}Dy. *Phys. Rev. A* **92**, 22703 (2015).
54. Wang, R. R. W. & Bohn, J. L. Anisotropic thermalization of dilute dipolar gases. *Phys. Rev. A* **103**, 063320 (2021).
55. Wang, R. R. W., Sykes, A. G. & Bohn, J. L. Linear response of a periodically driven thermal dipolar gas. *Phys. Rev. A* **102**, 33336 (2020).
56. Sadeghpour, H. R. et al. Collisions near threshold in atomic and molecular physics. *J. Phys. B* **33**, R93–R140 (2000).

Methods

Thermalization model. We fit the temperature and density evolution with a set of differential equations[26]:

$$\begin{aligned}\dot{n} &= -K_{\mathrm{L}}\left(T_y + 2T_x\right) n^2 - \tfrac{n}{2T_y}\dot{T}_y - \tfrac{n}{2T_x}\dot{T}_x \\ \dot{T}_y &= \tfrac{n}{4}K_{\mathrm{L}}\left(-T_y + 2T_x\right) T_y - \tfrac{2\Gamma_{\mathrm{th}}}{3}\left(T_y - T_x\right) + c_y \\ \dot{T}_x &= \tfrac{n}{4}K_{\mathrm{L}}T_yT_x + \tfrac{\Gamma_{\mathrm{th}}}{3}\left(T_y - T_x\right) + c_x.\end{aligned} \tag{3}$$

Γ_{th} is defined in equation (1) with $v = \sqrt{16k_{\mathrm{B}}(T_y + 2T_x)/(3\pi m)}$. K_{L} describes the two-body loss, and c_y and c_x are background heating rates. The model captures the two main contributions to the observed temperature evolution: (1) the elastic dipolar collisions described by the term proportional to Γ_{th} and (2) the effects on the temperature from the reactive loss described by the first term related to K_{L}.

The model has two assumptions for simplicity. First, we assume a similar reaction coefficient K_{L} for molecules colliding along different directions with respect to the dipole, which is valid in the vicinity of E_{S} (ref. [44]). Second, the temperatures of the two unmodulated directions x and z remain identical during the thermalization process. Systematic error introduced by this assumption is maximized at an angle of 45°, where the thermalization speed between y, x and y, z differs the most. Because the thermalization between y, z is much slower, adopting this assumption leads us to underestimate the thermalization rate around 45°.

Data analysis. For each θ, we image the molecules at several hold times between 0.05 and 10 s, at several times-of-flight between 1.5 and 8.2 ms, and with and without parametric heating. To minimize the systematic effects from slow drift in experimental conditions, we randomize the order in which the data is taken. For each hold time and heating condition, we fit the temperatures T_x and T_y and average density n, assuming free expansion of the cloud. Estimated values and their covariance matrices are obtained via bootstrapping. We fit the temperature and density decay curves to equation (3), treating K_{L}, N_{coll}, c_x, c_y and the initial temperatures and densities as fit parameters. To estimate confidence intervals on the fit parameters, we generate 100 synthetic datasets by independently drawing new temperatures and densities at each time point from a multivariate normal distribution. The reported parameters and confidence intervals represent the median and the intervals containing 68% of the trials. This approach lets us examine correlations between the different fit parameters. An example fit is shown in Extended Data Fig. 1a for $\theta = 45°$. The fit yields $N_{\mathrm{coll}} = 1.57(14)$, $K_{\mathrm{L}} = 3.8(3)\times10^{-7}\,\mathrm{cm^3\,s^{-1}\,K^{-1}}$.

Extended Data Fig. 1b shows the fitted result for 100 synthetic datasets. The small correlation of −0.26 between N_{coll} and K_{L} indicates that the fitting distinguishes between the thermalization and two-body loss well.

Extended Data Fig. 1c shows the extracted loss rate K_{L} versus θ. Although the measured K_{L} seems to be anti-correlated with N_{coll}, we find that the observed variation of K_{L} is not drastic enough to cause a substantial change to the extracted N_{coll}. This weak modulation of K_{L} could be caused by daily technical drifts on the electric field strength or residual field gradient, or contributions of the higher partial waves in the two-body collisions which may cause a higher K_{L} around $\theta \approx 54°$ where the shielding barrier is weak.

Temperature measurement. Temperatures are measured by fitting the Gaussian width of the cloud after time-of-flight expansion. To image the molecules, the electric field $\mathbf{E}$ is ramped from $\mathbf{E}_{\mathrm{S}}$ back to $\mathbf{E}_{\mathrm{STIRAP}}$ after the hold time. The molecules are then transferred to $|0,0\rangle$ and dissociated for imaging. The changes in the bias field and molecular rotational state result in changes to the molecular polarizability and, consequently, the trapping potential. To obtain accurate temperatures of the molecular gas during the thermalization process, we correct for such systematics as detailed below.

Transferring from $|1,0\rangle$ to $|0,0\rangle$ while the molecules are still in the trap causes an instantaneous change of the trapping potential and thus breathing of the cloud, which would introduce errors in the measured temperatures. We avoid this issue by performing the rotational state transfer and STIRAP during the time of flight.

The ramp down of the electric field from the measurement condition to $\mathbf{E}_{\mathrm{STIRAP}}$ modifies the trapping potential due to the polarizability change of $|1,0\rangle$ molecules with the bias field. Because this ramp is adiabatic with respect to the single-particle trapping periods along all spatial directions, the resultant adiabatic compression/decompression modifies the molecular temperature. We calculate the actual temperatures T_i during the thermalization process from the measured temperature T_i^{m} by

$$T_i = \left(\frac{\omega_i^{\mathrm{S}}}{\omega_i^{\mathrm{STIRAP}}}\right) T_i^{\mathrm{m}} \tag{4}$$

Here, ω_i^{S} and $\omega_i^{\mathrm{STIRAP}}$ are the trapping frequencies along i at $\mathbf{E}_{\mathrm{S}}$ and $\mathbf{E}_{\mathrm{STIRAP}}$, respectively. The trapping frequencies are calibrated by measuring the parametric heating resonances at each θ. The temperatures reported in this Article are T_i.

Data availability

The data that support the findings of this study are available from the corresponding author upon reasonable request. Source data are provided with this paper.

Acknowledgements

We acknowledge funding from ARO-MURI, AFOSR-MURI, DARPA DRINQS, NSF QLCI OMA–2016244, NIST, and NSF grant no. 1806971. L.L. and G.Q. acknowledge funding from FEW2MANY-SHIELD project no. ANR-17-CE30-0015 from Agence Nationale de la Recherche. We thank L. R. Liu for reading the manuscript.

Author contributions

J.-R.L., W.G.T., K.M., C.M., G.V., L.D.M. and J.Y. contributed to the experimental measurements. L.L. and G.Q. calculated the effective intermolecular potential. R.R.W.W. and J.L.B. calculated the anisotropic thermalization rate. All authors discussed the results, contributed to the data analysis and worked on the manuscript.

Competing interests

The authors declare no competing interests.

Additional information

Extended data is available for this paper at https://doi.org/10.1038/s41567-021-01329-6.

Supplementary information The online version contains supplementary material available at https://doi.org/10.1038/s41567-021-01329-6.

Correspondence and requests for materials should be addressed to J.-R.L. or J.Y.

Reprints and permissions information is available at www.nature.com/reprints.

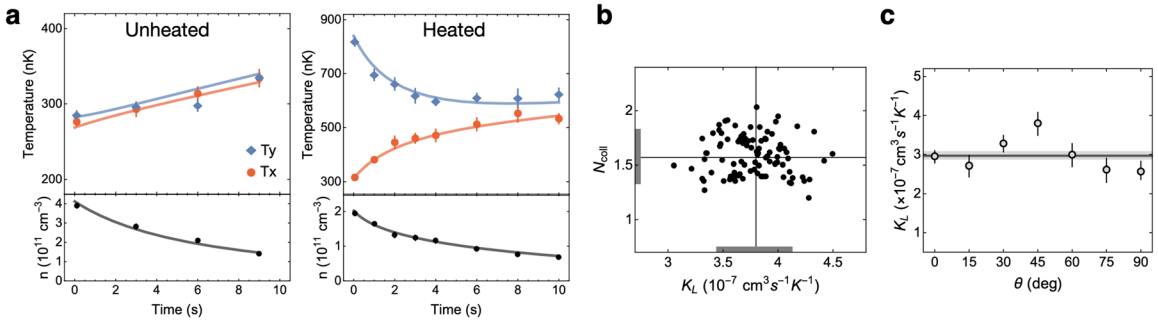

Extended Data Fig. 1 | Fitting experimental data with the model. The figure shows the fit results for $\theta = 45°$. **a**, Fitting of the unheated and heated data. **b**, Fitted K_L and N_{coll} for 100 synthetic datasets. We extract a correlation of −0.26 between the two fitted parameters, indicating that the fitting can distinguish between two-body loss and thermalization. The black solid lines are the median of all the fitted results from the synthetic datasets for N_{coll} and K_L, while the gray lines on the axis represent 68% confidence interval of the fitted results. This median and 68% confidence are reported in the main text. **c**, Extracted loss coefficient K_L versus θ. The line and shaded region indicate the mean value of K_L and its standard error.